Helium-ion-induced radiation damage in LiNbO₃ thin-film electro-optic modulators

Hsu-Cheng Huang,[1,*] Jerry I. Dadap,[2] Girish Malladi,[3] Ioannis Kymissis,[1] Hassaram Bakhru,[3] and Richard M. Osgood, Jr.[1,2]

[1]*Department of Electrical Engineering, Columbia University, New York, New York, 10027, USA*
[2]*Department of Applied Physics and Applied Mathematics, Columbia University, New York, New York, 10027, USA*
[3]*College of Nanoscale Science and Engineering, SUNY at Albany, Albany, New York 12203, USA*
[*]*hh2362@columbia.edu*

Abstract: Helium-ion-induced radiation damage in a LiNbO₃-thin-film (10 µm-thick) modulator is experimentally investigated. The results demonstrate a degradation of the device performance in the presence of He$^+$ irradiation at doses of $\geq 10^{16}$ cm^{-2}. The experiments also show that the presence of the He$^+$ stopping region, which determines the degree of overlap between the ion-damaged region and the guided optical mode, plays a major role in determining the degree of degradation in modulation performance. Our measurements showed that the higher overlap can lead to an additional ~5.5 dB propagation loss. The irradiation-induced change of crystal-film anisotropy $(n_o - n_e)$ of ~36% was observed for the highest dose used in the experiments. The relevant device extinction ratio, $V_\pi L$, and device insertion loss, as well the damage mechanisms of each of these parameters are also reported and discussed.

©2014 Optical Society of America

OCIS codes: (130.3730) Lithium niobate; (160.2100) Electro-optical materials; (230.2090) Electro-optical devices; (230.4110) Modulators.

References and links

1. L. Arizmendi, "Photonic applications of lithium niobate crystals," Phys. Status Solidi A **201**(2), 253–283 (2004).
2. M. Levy, R. M. Osgood, R. Liu, L. E. Cross, G. S. Cargill, A. Kumar, and H. Bakhru, "Fabrication of single-crystal lithium niobate films by crystal ion slicing," Appl. Phys. Lett. **73**(16), 2293 (1998).
3. P. Rabiei and P. Gunter, "Optical and electro-optical properties of submicrometer lithium niobate slab waveguides prepared by crystal ion slicing and wafer bonding," Appl. Phys. Lett. **85**(20), 4603–4605 (2004).
4. P. Rabiei, J. Ma, S. Khan, J. Chiles, and S. Fathpour, "Heterogeneous lithium niobate photonics on silicon substrates," Opt. Express **21**(21), 25573–25581 (2013).
5. L. Chen, M. G. Wood, and R. M. Reano, "12.5 pm/V hybrid silicon and lithium niobate optical microring resonator with integrated electrodes," Opt. Express **21**(22), 27003–27010 (2013).
6. J. Capmany and D. Novak, "Microwave photonics combines two worlds," Nat. Photonics **1**(6), 319–330 (2007).
7. R. C. Williamson and R. D. Esman, "RF Photonics," J. Lightwave Technol. **26**(9), 1145–1153 (2008).
8. W. J. Bock, I. Gannot, and S. Tanev, eds., *Optical Waveguide Sensing and Imaging* (Springer, 2008).
9. K. K. Wong, ed., *Properties of Lithium Niobate* (INSPEC, The Institution of Electrical Engineers, 2002).
10. H.-C. Huang, J. I. Dadap, O. Gaathon, I. P. Herman, R. M. Osgood, Jr., S. Bakhru, and H. Bakhru, "A micro-Raman spectroscopic investigation of He$^+$-irradiation damage in LiNbO₃," Opt. Mater. Express **3**(2), 126–142 (2013).
11. H.-C. Huang, J. I. Dadap, I. P. Herman, H. Bakhru, and R. M. Osgood, Jr., "Micro-Raman spectroscopic visualization of lattice vibrations and strain in He$^+$- implanted single-crystal LiNbO₃," Opt. Mater. Express **4**(2), 338–345 (2014).
12. E. I. Drummond, "Resistance of Ti:LiNbO3 devices to ionising radiation," Electron. Lett. **23**(23), 1214–1215 (1987).
13. C. D'Hose, E. Cassan, J. Baggio, O. Musseau, and J. L. Leray, "Electrical and optical response of a Mach-Zehnder electrooptical modulator to pulsed irradiation," IEEE Trans. Nucl. Sci. **45**(3), 1524–1530 (1998).
14. E. W. Taylor, "Ionization-induced refractive index and polarization effects in LiNbO₃:Ti directional coupler waveguides," J. Lightwave Technol. **9**(3), 335–340 (1991).
15. R. T. Schermer, F. Bucholtz, C. A. Villarruel, J. Gil Gil, T. D. Andreadis, and K. J. Williams, "Investigation of electrooptic modulator disruption by microwave-induced transients," Opt. Express **17**(25), 22586–22602 (2009).

16. A. Ofan, O. Gaathon, L. Vanamurthy, S. Bakhru, H. Bakhru, K. Evans-Lutterodt, and R. M. Osgood, "Origin of highly spatially selective etching in deeply implanted complex oxides," Appl. Phys. Lett. **93**(18), 181906 (2008).
17. T. A. Ramadan, M. Levy, and R. M. Osgood, Jr., "Electro-optic modulation in crystal-ion-sliced z-cut LiNbO$_3$ thin films," Appl. Phys. Lett. **76**(11), 1407 (2000).
18. J. Ziegler, 2008, *http://www.srim.org*.
19. R. M. Roth, D. Djukic, Y. S. Lee, R. M. Osgood, S. Bakhru, B. Laulicht, K. Dunn, H. Bakhru, L. Wu, and M. Huang, "Compositional and structural changes in LiNbO$_3$ following deep He$^+$ ion implantation for film exfoliation," Appl. Phys. Lett. **89**(11), 112906 (2006).
20. A. Ofan, O. Gaathon, L. Zhang, K. Evans-Lutterodt, S. Bakhru, H. Bakhru, Y. Zhu, D. Welch, and R. M. Osgood, "Twinning and dislocation pileups in heavily implanted LiNbO$_3$," Phys. Rev. B **83**(6), 064104 (2011).
21. A. Ofan, L. Zhang, O. Gaathon, S. Bakhru, H. Bakhru, Y. Zhu, D. Welch, and R. M. Osgood, "Spherical solid He nanometer bubbles in an anisotropic complex oxide," Phys. Rev. B **82**(10), 104113 (2010).
22. G. L. Destefanis, J. P. Gailliard, E. L. Ligeon, S. Valette, B. W. Farmery, P. D. Townsend, and A. Perez, "The formation of waveguides and modulators in LiNbO$_3$ by ion implantation," J. Appl. Phys. **50**(12), 7898 (1979).
23. W. D. Johnston, Jr., "Optical Index Damage in LiNbO$_3$ and Other Pyroelectric Insulators," J. Appl. Phys. **41**(8), 3279 (1970).
24. S. M. Kostritskii and P. Moretti, "Micro-Raman study of defect structure and phonon spectrum of He-implanted LiNbO$_3$ waveguides," Phys. Status Solidi C **1**(11), 3126–3129 (2004).
25. M. C. Teich and B. E. A. Saleh, *Fundamentals of Photonics* 2nd Ed. (John Wiley & Sons, Inc, 2007).
26. P. Bindner, A. Boudrioua, P. Moretti, and J. C. Loulergue, "Refractive index behaviors of helium implanted optical planar waveguides in LiNbO$_3$, KTiOPO$_4$ and Li$_2$B$_4$O$_7$," Nucl. Instrum. Meth. B **142**(3), 329–337 (1998).
27. J. Rams, J. Olivares, P. J. Chandler, and P. D. Townsend, "Mode gaps in the refractive index properties of low-dose ion-implanted LiNbO$_3$ waveguides," J. Appl. Phys. **87**(7), 3199–3202 (2000).
28. A. Boudrioua, J. C. Loulergue, F. Laurell, and P. Moretti, "Nonlinear optical properties of (H$^+$, He$^+$)- implanted planar waveguides in z-cut lithium niobate: annealing effect," J. Opt. Soc. Am. B **18**(12), 1832–1840 (2001).
29. F. Chen, X.-L. Wang, and K.-M. Wang, "Development of ion-implanted optical waveguides in optical materials: A review," Opt. Mater. **29**(11), 1523–1542 (2007).
30. L. C. Feldman and J. W. Mayer, *Fundamentals of Surface and Thin Film Analysis* (North-Holland, 1986).

1. Introduction

Because of its remarkable linear and nonlinear optical properties, lithium niobate (LiNbO$_3$) remains a key material for many types of photonic devices, which are widely used for applications in microwave telecommunications and data transmission [1]. Its large electro-optic (EO) coefficients (r$_{33}$ ~31 pm/V), excellent optical transparency in the telecom bands (~1.30 μm – 1.65 μm), and its electrically insulating properties make this crystal extensively employed in guided-wave optoelectronics. Films can be fabricated by etching and lift off (generally ~5 – 10 μm in thickness) using crystal ion slicing (CIS) [2] or they can be fabricated using wafer bonding with "smart cut" methods (generally for films with thickness <1 μm) [3]. These thinned materials make it possible to realize compact optical modulators with reduced size, weight, and power (SWaP) [4, 5].

Despite its outstanding properties for EO devices, less is known about the robustness of LiNbO$_3$ and its relevant EO device parameters in the presence of radiation bombardment or under extreme environment. Clearly this is an important issue since surface irradiation is integral to several approaches to LiNbO$_3$ material and device fabrication, including ion etching, implanted waveguides, and ion slicing, and an understanding of the resulting damage is essential to analyzing the performance of these materials. In addition, radiation hardness is important for many applications employing LiNbO$_3$ devices such as EO modulators or converters used in optical communications and networking technologies for radar-system antenna-remoting or in wireless and satellite applications [6, 7]. In particular, these applications are currently being considered for use in environments, which expose systems to high-energy ionizing radiation (e.g. in space or nuclear-power generation), or in the presence of an intense EMP (electromagnetic pulse) exposure [8]. In short, research on light-ion irradiation effects provides insight into the robustness of devices, such as modulators (studied here) and the corresponding damage mechanisms for degradation in device performance.

Prior studies have shown that the material properties of both doped and undoped bulk LiNbO$_3$ can be affected by bombardment with neutrons, electrons, X- and γ-rays [9]. In fact, light-ion bombardment using a clear well-understood model system such as LiNbO$_3$ and a

chemically inert bombardment species (He) provides an ideal approach to study radiation effects in complex-oxide EO devices. The damage from such bombardment includes the formation of point defects, lattice disorder, surface blistering, and irradiation-induced strain [10, 11]. In addition, there have been limited reports of the radiation hardness of some Ti:LiNbO$_3$ devices, such as Mach-Zehnder optomodulators and directional couplers. These studies have shown that the devices are radiation-resistant to X-rays up to a dose of ~10^5 rad [12], while damage due to high-energy electrons (~16 – 17 MeV) is dependent on the electron irradiation rate [13, 14]. Schermer *et al.* also reported dielectric breakdown and thermo-optic damage from high-power microwave (HPM) pulses, showing that prolonged resistive heating will result in both transient and possibly permanent damage of an electro-optic modulator [15]. The above pioneering research provides useful information and insight into the robustness of bulk materials; nevertheless, a comprehensive study of radiation damage on thinned, sliced devices and their corresponding EO responses has not yet been reported.

In this paper, we study helium-ion-induced radiation damage to a 10-μm-thick LiNbO$_3$ thin-film modulator. The device characteristics for electro-optic modulation, including extinction ratio and insertion loss, are compared for virgin and irradiated films. It is found that ion-bombardment-induced strain and scattering from interstitials and crystal defects give rise to the degradation of device modulation. In addition, we find that the degree of overlap between guided modes and the damaged regions plays an important role in the degradation of device performance.

2. Experimental and results

LiNbO$_3$ thin films (LNTF) were fabricated by using crystal ion slicing [2]. The congruent 500-μm-thick Z-cut samples (Crystal Technology) were first implanted by He$^+$ at 3.8 MeV with a dose of 5×10^{16} cm^{-2}. The implantation process was carried out in the presence of water cooling and with a 7-degree tilt of the sample face to the beam axis to prevent ion channeling. After implantation, the samples were diced to the desired size (several mm^2) and the facets for optical-in and -out coupling were polished to a flatness of ~λ/10. Subsequently the samples were annealed at 250°C for 30 minutes for thermal activation and then placed in a ~5% hydrofluoric (HF) acid etching bath for several hours. Because of the high etch selectivity in the buried sacrificial layer [16], the etching results in exfoliation of a ~10 μm-thick single-crystal-LN film. Post lift-off annealing (PLA) was then carried out in a furnace at 600°C for 10 hours in a laboratory-atmosphere ambient to remove any residual stress [17].

After PLA, the freestanding CIS film was bonded to an oxidized Si wafer by silver paint, which also acted as a ground electrode. Subsequently, ~10 nm-thick chromium and ~40 nm-thick gold electrodes were thermally deposited on top of the film to form the top electrode. Shadow masking was used for this patterning step to prevent electrical shorting by undesired metallization on the facets. Note that the facets for light coupling were "suspended" over the edge of the substrate so as to present a short cantilevered section of crystal on either side of the substrate. With this geometry, coupling loss to the facet was significantly reduced. Figure 1(a) shows an example of the CIS film (LNTF) and its parent crystal. Figures 1(b) and 1(c) are the optical images of the side view of the film before and after PLA; it is clear from the figure that before annealing, the residual stress results in bending of the film since reflected light on the substrate can be seen clearly under the film [Fig. 1(b)]. During PLA, the stress is released and the film becomes planar [Fig. 1(c)]. Figure 1(d) is a SEM picture of the device. The upper inset is the corresponding optical image showing the effective length of the modulator to be ~2.1 mm. The lower inset shows the cross section at the light-coupling facet.
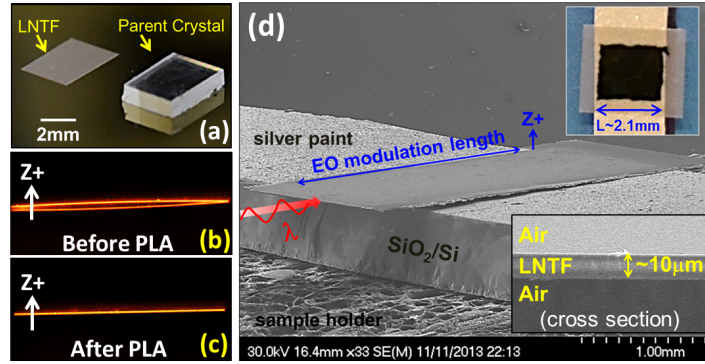
Fig. 1. (a) Examples of a CIS LiNbO$_3$ thin film (~10 μm thick) and its parent crystal; (b) and (c) are optical images of a side view of the CIS film before and after PLA (Post Liftoff Annealing). It is clear that before PLA [Fig. 1(b)], the as-exfoliated CIS film is stressed, showing the reflection of the film on the underlying substrate. After annealing at 600°C for 10 hours, the stress is fully released and a recovered, planar film is obtained [Fig. 1(c)]. Panel (d) displays an SEM image showing the thin-film EO modulator. The upper inset is the corresponding optical image; the lower image is an SEM micrograph showing the device cross section at its input. Note that the facets of the device are "suspended" in air for better optical coupling efficiency.

Measurement of the Pockels effect was carried out using free-space in-coupling. Figure 2 shows the optical setup, in which the tunable-laser beam was coupled into the device at its input and coupled out at the output for transmission measurements. In particular, the thin-film waveplate is placed between two crossed polarizers, with their polarization axes tilted at 45° with respect to the crystal Z axis and oriented 90° between each other so as to result in intensity modulation of the output. The wavelength-tunable collimated beam is focused by a 10 × microscope objective lens (N.A. ~0.3) with a spot size of ~10 μm placed at the input of the film modulator. The outgoing light is collected by a 7 × lens. This lens is followed by a pellicle beamsplitter, which transmits ~90% of light to a germanium (Ge) photodetector and reflects ~10% of light into an IR camera to observe coupling alignment. The input coupling was adjusted such that the fundamental slab mode was excited in the film. To demonstrate electro-optic modulation, an external voltage was applied directly to the metallic electrodes by a flexible probe. Optical measurements were then carried out to determine the device operating parameters, including its extinction ratio, V$_\pi$L and insertion loss.

Figure 3 shows the results of measurement of a typical device performance prior to irradiation. For the measurements shown in Fig. 3(a), the input wavelengths were tuned over the range from 1570 nm to 1585 nm in wavelength steps of 0.5 nm. For each data point, the laser was first stepped to the wavelength of choice and then the transmitted power was measured in the absence of an external voltage (black curve) and then with an applied voltage of V = 30 V (red curve). For Fig. 3(b), the input wavelength was fixed at 1570 nm, and the transmitted power was measured at each value of external voltage when the voltage was stepped from 0 V to 60 V with a step of 1 V. Using this procedure, for this unirradiated LNTF modulator, an 8 – 10 dB extinction ratio and V$_\pi$L ~7.5 V-cm were obtained. Note that the device performance can be further enhanced by, for example, depositing thin SiO$_2$ buffer layers on both sides of the film to reduce the absorption loss in the metal electrodes. However the research in this paper focused on investigating radiation damage; thus our study considered only an analysis of device-performance changes in the presence of radiation.
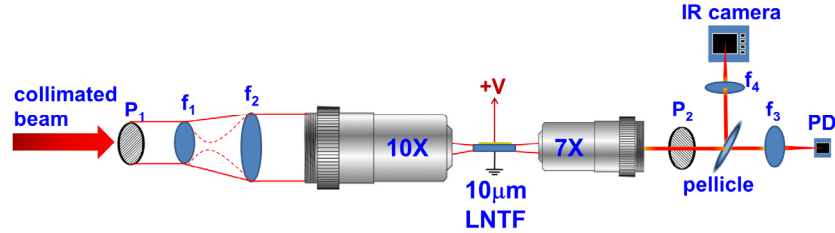
Fig. 2. Schematic of the experimental setup for free-space coupling. The collimated beam is focused by a 10 × objective lens to achieve a spot size of ~10 μm at the device input. The outgoing light is then collected by another 7 × lens. A pellicle beamsplitter was used so that ~10% of light is reflected to an IR camera for the observation of coupling while ~90% of light is transmitted to the photodetector. The electro-optic measurement is performed by applying an external voltage directly to the top electrode of the film. P: polarizer; f: lens; PD: photodetector.
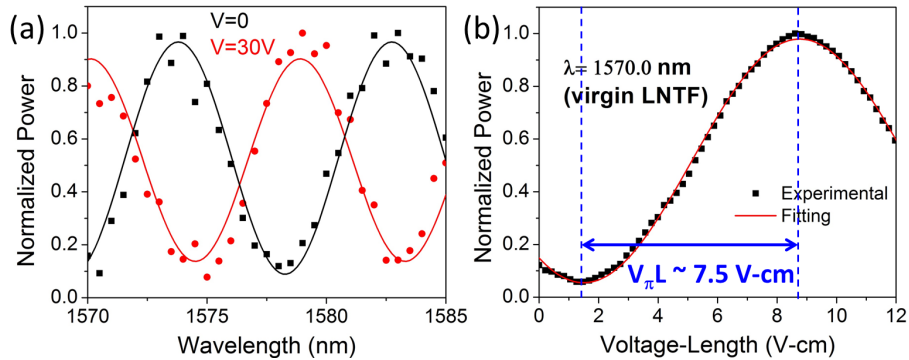

Fig. 3. (a) and (b) display examples of the electro-optic modulation using virgin LNTF: a ~10 dB extinction ratio (modulation depth of ~90%) with ~7.5 V-cm $V_{\pi}L$ parameters were measured (see text for a description of the measurement protocol). A sine-squared function was used for the data fitting (solid lines). The device overall length is ~3.5 mm, with an effective electrode length of ~2.1 mm.

The CIS-film (~10 μm) modulators were subsequently irradiated by He$^+$ at different energies and doses to study the effect of radiation on modulator performance. For convenience, irradiation was performed under the same conditions as for implantation of bulk materials for slicing. Note that to ensure homogeneous irradiation, the beam current during the implant was maintained at ~280 ± 10 nA/cm^2. Two energies were chosen: 2.3 MeV and 3.6 MeV. From *SRIM* (*Stopping and Range of Ions in Matter*) [18] calculations, the stopping ranges of 2.3 and 3.6 MeV He$^+$ are ~5 μm (in the middle of the film) and ~9 μm below the top surface, with straggle distances of ~300 nm and ~400 nm, respectively. After irradiation, the device performance was then tested again and compared that of the unirradiated modulator. Also note that to alleviate any possibility of heating during irradiation, thus giving rise to electrode damage, the irradiation performed in our experiments was raster-scanned under water-cooled environment.

Figure 4 show the modulator appearance and performance after irradiation. Figures 4(a) and 4(b) are optical images of the thin-film modulators after 3.6 MeV He$^+$ irradiation at doses of 1×10^{16} cm^{-2} and 5×10^{16} cm^{-2}, respectively. Earlier work [17] had shown that this form of He$^+$ irradiation gives rise to a strained thin film. In addition, in our experiments, after a bombardment dose of 5×10^{16} cm^{-2} He$^+$, this built-in stress is sufficiently high, in some cases, that the film partially cracks. Figures 4(c) and 4(d) display the modulator output signal for three values of irradiation when different input wavelengths [Fig. 4(c)] and voltages [Fig. 4(d)] are used. The inset in Fig. 4(c) shows the normalized transmitted power for each irradiation case. The performance degrades as the dose is increased. For example, our initial

experiments showed that a He^+-2×10^{16} cm^{-1}-dose irradiation led to an additional waveguide loss of ~9 dB, a ~5 dB lower extinction ratio, and a ~73% degraded $V_\pi L$ value for the modulator.

A careful consideration of results, such as in Figs. 4, 5, and Table 1 described below, shows that in our study, there are two sources of modulator damage. The first is crystal (lattice) damage from the He ion-beam interactions. This damage leads to the formation of point defects, dislocations, and related extended defects, all of which increase optical scattering [19]. In addition, during implantation at doses of $> 0.5 \times 10^{16}$ cm^{-2}, ~5 nm He bubbles self-assemble in the solid lattice within the stopping region [20]. In the presence of higher-temperature annealing, such as the T = 600°C annealing process used here, larger-scale ~100 nm He bubbles are formed from the coalescence of the nascent 5 nm bubbles, which have a significant Rayleigh optical scattering cross section [21]. Note that without proper post-irradiation annealing, the presence of these defects and the associated lattice disorder can shift the refractive index profile of the guide and hence induce changes in the modal profiles, resulting in leaky modes [22]. Such altered modal structures manifest themselves in part as light scattered away from the guiding region.

To illustrate the role of this scattering, a 633-nm-wavelength probe was used for the observation of visible scattered light in the waveguide and observed through the top surface of the film. In the presence of 3.6 MeV He^+ irradiation to a dose of 2×10^{16} cm^{-2}, strong light scattering through the top surface of the thin-film modulator is seen; see Figs. 5(a) and 5(b).
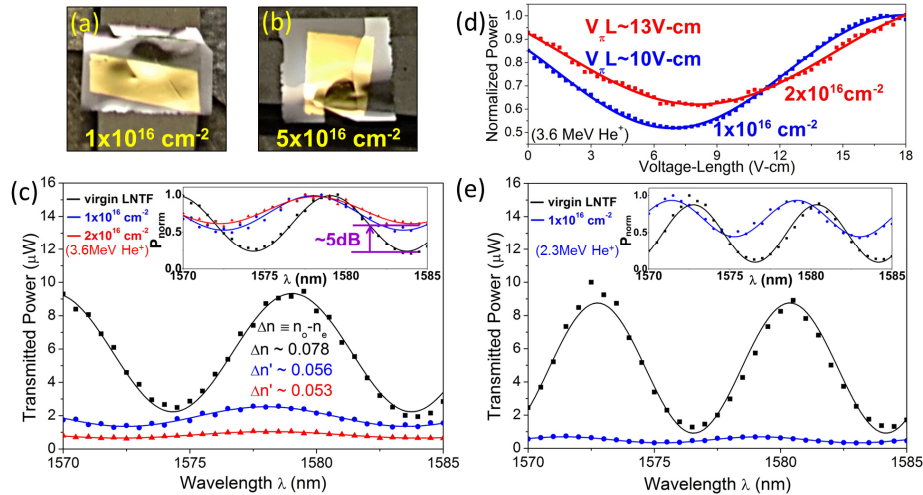

Fig. 4. Panels (a) and (b) are optical images of the modulators after 3.6 MeV He^+ irradiation at a dose of $\geq 10^{16}$ cm^{-2}. It is clear that the film is strained and, when the dose is 5×10^{16} cm^{-2}, the stress is large enough to result in film fracture. Panels (c) and (d) are measured data showing that as the dose is increased, device performance degrades, *viz* a ~9 dB additional waveguide loss, ~5 dB lower extinction ratio and a ~73% increased $V_\pi L$ value indicating degradation for a dose of 2×10^{16} cm^{-2}. The inset in Fig. 4(c) shows the degradation of the extinction ratio using the normalized transmitted power for each irradiated condition, where P_{norm} is the normalized transmitted power. Figure 4(e) and the inset show a 2.3 MeV He^+ irradiated case at a dose of 1×10^{16} cm^{-2}. Compared with 3.6 MeV He^+ with the same irradiation dose [i.e. 1×10^{16} cm^{-2}, blue curve in panel (c)], additional ~5.5 dB propagation loss is observed for 2.3 MeV He^+ irradiation, due to higher overlap of the damaged region (in the center) and the optical guided mode.

In addition, this scattering also increases the device propagation loss over that of the unirradiated device. For example, measurements of the loss in transmission show that it increases from ~2 dB in the implanted device to ~7.5 dB for a dose of 1×10^{16} cm^{-2}, to ~11.3 dB for a dose of 2×10^{16} cm^{-2}, and to ~16 dB for a dose of 5×10^{16} cm^{-2} at a beam energy of

3.6 MeV. In addition, our experiments showed that, in comparison with 3.6 MeV He[+] irradiation, 2.3 MeV irradiation for the same dose yields higher propagation loss (see Fig. 4(e) where an additional propagation loss of ~5.5 dB was observed). This result is attributed to the energy-dependent depth of damage, which results in the spatial overlap between the optical guided mode and the He^{+}-damaged region, since the 2.3 MeV He[+] ions stop in the center of the film, while 3.6 MeV He[+] ions stop at the bottom. Thus when a Gaussian beam is coupled into the center of the film, the higher overlap leads to stronger light scattering from the damaged region for the 2.3 MeV case, therefore resulting in greater loss in the guided mode.

The second source of modulator degradation is the material birefringence change caused by irradiation. This change can be attributed to both an increase in strain within the crystal and a partial loss of crystallinity in the stopping region. Strain is induced in the crystal during He^{+} irradiation, due to the presence of interstitial He, nm-scale nascent clusters of He, or through the formation of larger bubbles [21]. This strain can lead to a significant change in the crystal birefringence following ion irradiation. In addition, He^{+} irradiation is also known via optical and electrical microscopy [20] to generate a thin region with partially degraded crystallinity. Such a region will also have a different (lower) birefringence than the unirradiated crystal.

In order to examine the effects of this birefringence, measurements were made of the polarization response as a function of the input wavelength for unirradiated and irradiated films. Again, two ion energies were used. The results of this measurement are illustrated using the data in Fig. 4(c), where it is seen that after irradiation, a change occurs in the phase of the modulation envelope and a decrease in the dependence of the output power on wavelength. In addition, the depth of modulation (or extinction ratio) is substantially reduced and that higher dose increases the reduction in modulation depth; see the inset in Fig. 4(c). Figure 4(d) shows voltage-dependent modulation measurements at a wavelength of $\lambda = 1570$ nm; again notice that higher dose degrades the modulation depth. This degradation in the modulation is consistent with an irradiation-induced decrease in the intrinsic birefringence. Note that although the use of 2.3 MeV He[+] results in higher overlap with the optical mode, the measured $V_{\pi}L$ (~9.5 V-cm) is still comparable in magnitude to the value after 3.6 MeV He[+] irradiation (~10 V-cm) for the same dose (1×10^{16} cm^{-2}). Considering that electro-optic polarization is directly related to Raman susceptibility [23, 24], a micro-Raman edge scan at different depths was performed to resolve any irradiation-induced change in the active phonon modes [11]. The results (not presented here) show that these two energies, both having comparable straggle length with the thickness of the film, give rise to similar distributions of the built-in strain field (obtained from spectral shift) and crystalline damage (from linewidth broadening). Such comparable damage profiles indicate the two cases having similar overall changes of birefringence (discussed below) and EO coefficients (r_{33} and r_{31}). Thus, for these two cases, the voltage-dependent retardation would result in similar values of $V_{\pi}L$.

The irradiation-induced change in the intrinsic film birefringence can be further characterized using a quantity based on a measurement of the normalized birefringence of the LNTF modulator. In particular, it is known [25] that the phase retardation of polarized light propagating through a waveplate (birefringent material) is proportional to its index anisotropy or birefringence; this basic phenomenon allows us to measure this same quantity in our LNTF modulator using a measurement of the extinction ratio. Thus a sine-squared function $\sin^2[\frac{\pi L(n_o - n_e)}{\lambda_o}]$, corresponding to the power transmittance of the system, was used

to fit the measured normalized wavelength-dependent modulation and, hence, the change of the index anisotropy for the two indices $(n_o - n_e)$ induced by irradiation. Note that prior to irradiation, the LNTF sample had $(n_o - n_e)$ equal to ~ 0.078, which agrees well with the

theoretical value (~ 0.074) using the Sellmeier equation for $\lambda = 1570$ nm [9]. After He$^+$ irradiation with a dose of 2×10^{16} cm^{-2}, the difference $(n_o^{'} - n_e^{'})$ decreased to ~ 0.053. As the irradiation dose is increased, greater lattice distortion occurs due to an increase in the induced stress and defect clusters [10] such that the birefringence or anisotropy is decreased. Defining an isotropy factor (C), $C \equiv \dfrac{\Delta n - \Delta n'}{\Delta n} = \dfrac{(n_o - n_e) - (n_o^{'} - n_e^{'})}{(n_o - n_e)}$, we can find the degree of change of the anisotropy/birefringence. For example, $C \sim 0.32$ for our 2×10^{16} cm^{-2} He$^+$ fluence. This result indicates that, in the range of the wavelengths used in the experiments (telecom windows), $\sim 68\%$ of the material birefringence is preserved. Note that an optically isotropic material ($n_e^{'} = n_o^{'}$) will have a $C = 1$, and for our unirradiated LNTF, $C = 0$ ($\Delta n' = \Delta n$). Also before post-liftoff annealing, e.g. as shown in Fig. 1(b), high residual stress and radiation defects from 5×10^{16} cm^{-2} He$^+$ irradiation and the exfoliation process leads to a change in birefringence yielding a $C \sim 0.5$ [17]. The estimated error of $\sim \pm 2\%$ originates from uncertainty in measurement of the propagation length ΔL. In general, higher-dose irradiation results in greater change of anisotropy/birefringence, and the calculated C factor. The analysis is summarized in Fig. 5(c).
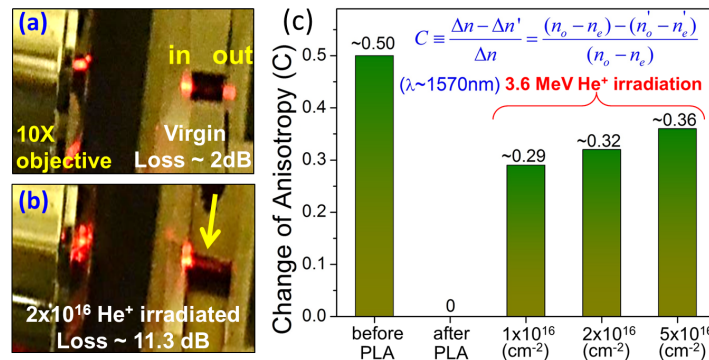

Fig. 5. (a) and (b): optical top-surface images of end-facet-coupled light using a visible (red) light source to directly observe scattering. (a): light coupled into an unirradiated LNTF sample; (b) light coupled into an irradiated thin film (2.3 MeV He$^+$ to a dose of 2×10^{16} cm^{-2}). In (b), the scattered light through the top surface of a thin-film modulator is readily seen (designated by a yellow arrow. See text for a discussion of the origin of the scattering. (c): The change of LNTF index anisotropy/birefringence under different conditions (wavelength $\lambda \sim 1570$ nm). PLA stands for Post Liftoff Annealing; see Figs. 1(b) and 1(c) for the corresponding optical images. After PLA, the thin-film modulator is irradiated with 3.6 MeV He$^+$ with different doses. It is clear that as the irradiation dose is increased, the damage of lattice structure is enhanced such that the change of anisotropy (C factor) is greater. Note that if the material is optically-isotropic, $C = 1$.

Several groups [26–28] have reported measurements of the index profile from He$^+$ implantation in bulk LiNbO$_3$ waveguides. These measurements show that for high-dose He$^+$ irradiation ($>10^{16}$ cm^{-2}), irradiation-induced lattice damage and strain give rise to a percent-level decrease in both n_o and n_e in the nuclear damage region. This phenomenon is sufficiently reproducible that it has been used to form an optical barrier for the confinement of guided light in high-quality optical waveguides [29]. Our measurements using *thin films* (C ~ 0.32 with $\lambda = 1570$ nm) show that under the similar implantation parameters, the preserved birefringence agrees well with literature values [26–28], if the appropriate wavelength dispersion is taken account (for example, in [28], C ~ 0.45 using second harmonic signals of $\lambda = 1060$ nm). The near coincidence of the change of birefringence in the ~ 10 μm-thick thin film and ~ 500 μm-thick bulk LiNbO$_3$ crystal is attributed to the fact that such index effects result from local structural changes and the induced stress fields, both of which are of

comparable magnitude in thicker samples. Note that since the stopping cross section scales with the projectile atomic number (Z) [30], radiation damage is expected to be greater if heavy-ion irradiation is used.

Finally, Table 1 summarizes the results of our measurements of He$^+$-irradiation damage in our LiNbO$_3$ thin-film EO modulators and the corresponding damage mechanisms to the device operating parameters. The reduced extinction ratio and the increased V$_\pi$L are also compared in the table to the values measured in the unirradiated case. It is clear from this table that both the *total dose* and the *distribution of that dose* with respect to the waveguide optical mode determine the degradation in extinction ratio, V$_\pi$L, and insertion loss in the presence of ionizing radiation, *viz* He$^+$.

Table 1. Summary of Device Parameters in the Absence and Presence of Different Irradiation Conditions and Examples of the Corresponding Damage Mechanisms

Thin Film (~10 μm thick)	Prototype	2.3 MeV	3.6 MeV He$^+$ dose (cm^{-2})			Damage Mechanism
		1×10^{16}	1×10^{16}	2×10^{16}	5×10^{16}	
Extinction Ratio (dB)	~8 – 10	~6.5 dB lowered	~4 dB lowered	~5 dB lowered	~6.2 dB lowered	1. Lattice disorder (strain) 2. Light scattering from interstitials
V$_\pi$L (V-cm)	~7.5	~9.5 (~27%↑)	~10 (~33%↑)	~13 (~73%↑)	N.A.*	1. Lattice disorder 2. Electrodes damage
Insertion Loss (dB)	~2	~13	~7.5	~11.3	~16	1. Absorption 2. Damage at interface 3. Light scattering

*films are partially cracked

3. Conclusions

In conclusion, He$^+$-induced radiation damage in 10-μm-thick LNTF modulators is investigated. Our results show that lattice disorder and stress give rise to the degradation of device performance for a dose $\geq 10^{16}$ cm^{-2}. The device performance, determined primarily by operating parameters, including extinction ratio, V$_\pi$L, and insertion loss, has a complex dependence on the energy and dose of the He$^+$ radiation. Two He$^+$ energies, corresponding to different stopping ranges, were used and measurements of films irradiated using these energies demonstrate that the degree of overlap between guided modes with damaged regions has a significant effect on the degree of achievable modulation. In particular, the less energetic He$^+$ ions at 2.3 MeV yielded significant insertion loss degradation than that from the more energetic 3.8 MeV He$^+$ ions due to the overlap of the stopping range with the waveguide mode. For a given or fixed ion energy, the degradation in operating parameters increased as the ion dose was increased. In addition, the device performance is influenced by scattering from interstitial damage states and irradiation-induced strain, further altering the optical anisotropy and the EO coefficients. Finally, note that, given the results of our research, it may be possible to redesign an electro-optical structure so as to make it sensitive to radiation damage. For example, the device modal structure could be reworked so as to make radiation alteration of the mode by ion bombardment a sensitive optical-detection scheme. The fundamental knowledge measured here can provide the information needed to design such a new instrument.